NAVAL POSTGRADUATE SCHOOL
Monterey, California

THESIS

INTEGRATED OPTICAL SIGMA-DELTA MODULATORS

by

Stephen J Ying

September, 1995

Thesis Advisor: Phillip E. Pace

Approved for public release; distribution is unlimited.

19960220 029

DTIC QUALITY INSPECTED 1

REPORT DOCUMENTATION PAGE

Form Approved
OMB No. 0704-0188

1. AGENCY USE ONLY *(Leave blank)*	2. REPORT DATE September, 1995	3. REPORT TYPE AND DATES COVERED Master's Thesis

4. TITLE AND SUBTITLE
INTEGRATED OPTICAL SIGMA-DELTA MODULATORS

5. FUNDING NUMBERS

6. AUTHOR(S) Stephen J Ying, LT USN

7. PERFORMING ORGANIZATION NAME(S) AND ADDRESS(ES)

Naval Postgraduate School
Monterey CA 93943-5000

8. PERFORMING ORGANIZATION REPORT NUMBER

9. SPONSORING/MONITORING AGENCY NAME(S) AND ADDRESS(ES)

Space and Naval Warfare Systems Command, Washington, D.C.

10. SPONSORING/MONITORING AGENCY REPORT NUMBER

11. SUPPLEMENTARY NOTES
The views expressed in this thesis are those of the author and do not reflect the official policy or position of the Department of Defense or the U.S. Government.

12a. DISTRIBUTION/AVAILABILITY STATEMENT

Approved for public release; distribution unlimited.

12b. DISTRIBUTION CODE

13. ABSTRACT *(maximum 200 words)*

Modern avionics equipment, such as super resolution direction-finding systems, now require resolutions on the order of 20 to 22 bits. Oversampled analog-to-digital converter architectures offer a means of exchanging resolution in time for that in amplitude and represent an attractive approach to implementing precision converters without the need for complex precision analog circuits. Using oversampling techniques based on sigma-delta modulation, a convenient tradeoff exists between sampling rate and resolution. One of the major advantages of integrated optics is the capability to efficiently couple wideband signals into the optical domain. Typically, sigma-delta processors require simple and relatively low-precision analog components and thus are well suited to integrated optical implementations. This thesis reviews the current sigma-delta methodology, the advantages of optical integrated circuits and presents the design of a second-order, integrated optical sigma-delta modulator. Simulation results for both a first and second order architecture are presented by evaluating the transfer characteristics numerically. Design parameters such as limit cycles are quantified and explained. Performance issues and future efforts are also considered.

14. SUBJECT TERMS
Sigma-delta Modulation, Optical Integrated Components, Analog-to-Digital Converters (ADCs)

15. NUMBER OF PAGES
53

16. PRICE CODE

17. SECURITY CLASSIFICATION OF REPORT	18. SECURITY CLASSIFICATION OF THIS PAGE	19. SECURITY CLASSIFICATION OF ABSTRACT	20. LIMITATION OF ABSTRACT
Unclassified	Unclassified	Unclassified	UL

INTEGRATED OPTICAL SIGMA-DELTA MODULATORS

Stephen J Ying
Lieutenant, United States Navy
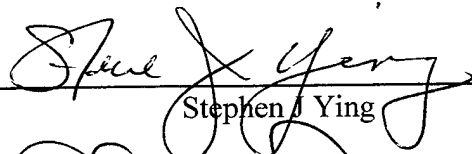B.S., Stanford University, 1990

Submitted in partial fulfillment of the
requirements for the degree of

MASTER OF SCIENCE IN ELECTRICAL ENGINEERING

from the

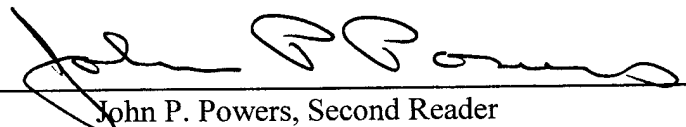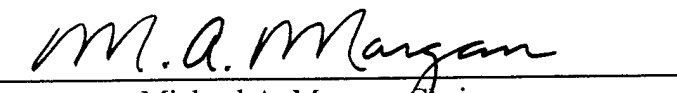## NAVAL POSTGRADUATE SCHOOL
September 1995

Author: _____
Stephen J Ying

Approved by: _____
Phillip E. Pace, Thesis Advisor

_____
John P. Powers, Second Reader

_____
Michael A. Morgan, Chairman,
Department of Electrical and Computer Engineering

ABSTRACT

Modern avionics equipment, such as super-resolution direction-finding systems, now require resolutions on the order of 20 to 22 bits. Oversampled analog-to-digital converter architectures offer a means of exchanging resolution in time for that in amplitude and represent an attractive approach to implementing precision converters without the need for complex precision analog circuits. Using oversampling techniques based on sigma-delta modulation, a convenient tradeoff exists between sampling rate and resolution. One of the major advantages of integrated optics is the capability to efficiently couple wideband signals into the optical domain. Typically, sigma-delta processors require simple and relatively low-precision analog components and thus are well suited to integrated optical implementations. This thesis reviews the current sigma-delta methodology, the advantages of optical integrated circuits and presents the design of a second-order, integrated optical sigma-delta modulator. Simulation results for both a first and second order architecture are presented by evaluating the transfer characteristics numerically. Design parameters such as limit cycles are quantified and explained. Performance issues and future efforts are also considered.

TABLE OF CONTENTS

ACKNOWLEDGEMENT

I. INTRODUCTION

A. BACKGROUND

Analog-to-digital converters (ADCs) are basic building blocks for a wide variety of digital systems. A partial list of ADC applications includes process control, automatic test equipment, video signal acquisition, audio recordings for compact disc and interfaces for personal computers. There exists a variety of approaches to the ADC design. One approach, known as delta modulation, involves the use of oversampling methods. First introduced in the 1940s, delta modulation uses oversampling and single-bit code words to represent the analog signals [Ref. 1]. The simplest approach counted the output bits from the delta modulator with a high bit representing a +1 and a low bit a −1. The output was then resampled at the Nyquist rate. Resolution proved to be a problem, since achieving adequate reproduction of speech signals required oversampling ratios of the order 5,000. More effective digital filtering was needed to prevent the high-frequency modulation noise from aliasing into the signal band when it was resampled at the Nyquist rate.

Unfortunately at that time, digital filters used for this purpose were prohibitively expensive. Candy proposed an interpolative technique for digital filtering [Ref. 2]. The idea was to digitize the signal through the use of a coarse quantizer and to cause the output to oscillate between the quantized levels at high speed so that its average value over the Nyquist interval was an accurate representation of the sampled value. The digital filters used to generate this average were inexpensive. On the other hand, these digital filters also proved to be reliable and fairly tolerant of circuit imperfections. The quantizers for these interpolating converters utilized a noise-shaping technique which measures the quantization error in one sample and subtracts it from the next input sample value [Ref. 3]. The most popular form of this noise-shaping technique is known as *sigma*

1

delta modulation. Sigma delta modulators employ integration and feedback in iterative loops to obtain high-resolution A/D conversions.

Specifically, a sigma delta modulator ($\Sigma\Delta$M) consists of an analog filter and a quantizer enclosed in a feedback loop [Ref. 4]. Together with the filter, the feedback loop acts to attenuate the quantization noise at low frequencies while amplifying the high-frequency noise. Since the signal is oversampled at many times the Nyquist rate, a digital low-pass filter may be used to remove the high-frequency quantization/modulation noise without affecting the signal band. This filtering usually involves a multi-stage decimation process since the output of the modulator represents the signal with the high-frequency modulation noise as well as its out-of-band components which dominate at the lower frequencies. In general, the smoothing characteristics involved in the decimation process require that the signal propagate through several filters and resampling stages. The first stage of decimation lowers the word rate to an intermediate frequency, where a filter removes the high-frequency modulation noise. A second low-pass filter is then used to attenuate the out-of-band components before the signal is resampled at its Nyquist rate. As the signal propagates through the filters and resampling stages, the word length increases in order to preserve the resolution. A more thorough discussion of multi-stage decimation and filtering can be found in [Ref. 1].

The transmission of coherent light through optical waveguides has been of great interest ever since the late 1960s. Through this interest emerged the concept of *integrated optics*, in which wires and radio links are replaced by light-waveguiding optical fibers and conventional electrical integrated circuits are replaced by miniaturized optical integrated circuits (OICs). Optical integrated components offer a number of advantages over their electronic counterparts. These advantages include large bandwidth, use of optical sources capable of high-speed switching (which is necessary for high PRFs), low power consumption, improved reliability and insensitivity to vibration and EMI. A key advantage is the increased characteristic bandwidth over electronic components. The carrier medium is a lightwave rather than an electrical current. Thus

the frequency limiting effects of capacitance and inductance can be avoided. Since electronic converters based on $\Sigma\Delta$ modulation require oversampling, their applicability is mainly limited to low and moderate signal frequencies. For instance, oversampling a 500 MHz wideband RF signal by a factor of 10 over the Nyquist rate would require a sample rate of 10 GHz, which is difficult to process in an all-electronic bandlimited system. Therefore the use of optical integrated components provides an attractive solution to the otherwise bandlimited electronic $\Sigma\Delta$ architecture.

B. PRINCIPLE CONTRIBUTIONS

This thesis describes a single-bit, integrated optical $\Sigma\Delta M$ approach. The $\Sigma\Delta$ modulation scheme is analyzed and reviewed in detail. First- and second-order single-bit, all-electronic modulators are modeled by functional blocks and simulated using MATLAB's SIMULINK software package. In the integrated optical $\Sigma\Delta$ architecture, conventional optical components are utilized to match each functional block according to its system transfer characteristic. The parameters of these optical integrated components are then optimized to achieve results matching those of the all-electronic design. The simulation results of the optical integrated $\Sigma\Delta Ms$ illustrate the feasibility of the integrated optical approach.

C. THESIS OUTLINE

In Chapter II, the all-electronic $\Sigma\Delta$ modulator is reviewed with both first- and second-order architectures being discussed. Analysis and simulation results for both the first- and second-order models are presented. Chapter III introduces an integrated optical architecture for a first- and second-order $\Sigma\Delta$ modulator. It explains the optical devices used for implementation and compares them at a component level to the all-electronic

design. Simulation results are presented and analyzed. Chapter IV details the relationship between oversampling and resolution and discusses in terms of the modulator's signal-to-noise ratio. Chapter V describes the computer software used to simulate the $\Sigma\Delta$ modulators. Finally, Chapter VI discusses issues concerning the current simulation model and presents suggestions for future efforts.

II. ALL-ELECTRONIC, SINGLE-BIT ΣΔ MODULATORS

A. FIRST-ORDER ΣΔM

A sampled-data equivalent of a first-order ΣΔM is shown in Figure 1. Because this is a sampled-data circuit, the integration is performed via an accumulator. The analog signal is assumed to be oversampled at well above the Nyquist frequency. This sampled input, x_i, is fed to the quantizer via the accumulator. The quantized output, which can be modeled as an approximation of the quantization error, is fed back and subtracted from the input. This quantized feedback signal forces the average value of the quantized output, y_i, to track the average value of the input signal. Any difference accumulates in the integrator and eventually corrects itself.
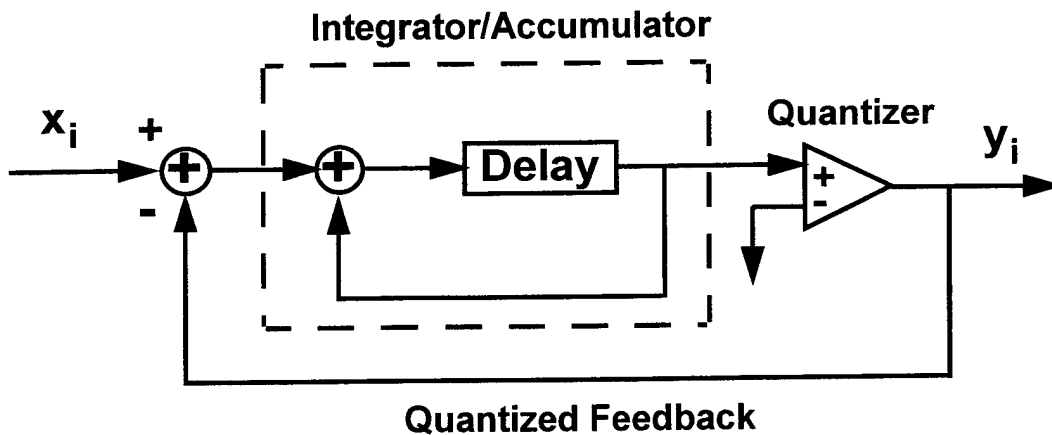
**Figure 1.** Block diagram of a 1st-order all-electronic ΣΔM.

The quantization error is subtracted from the input value and the difference becomes the input for the next cycle. After the process is repeated many times at high speed, an average of the digital outputs occurring in each sample time becomes a useful digital representation of the input signal. In a stable converter, the oscillations of the

quantized value are bounded, that is, the oscillations have a limit cycle. In general this quantization process can be performed over more than one quantization level [Ref. 1]. By this process, it can be seen that the speed of operation obviates the need for precise circuit elements. Precision in the quantization levels of the quantizer is not a stringent requirement since the average of the quantized output, y_i, will automatically be adjusted to agree with the sampled input analog signal, x_i. Therefore, the output of the $\Sigma\Delta$ modulation process can provide a high level of precision in the representation despite coarseness in the quantization levels.

The input/output transfer characteristics of the first-order $\Sigma\Delta M$ is plotted in Figure 2a. The signal oscillates between the quantized levels in such a manner that its local average equals the average input. For this example the input signal is ramped with 200 samples with a ±1 volt range. The comparator output voltage is ±1 volt with the threshold voltage set at zero volts. Figure 2b shows the undesirable limit cycles at the output of the accumulator. These simulation results are in agreement with previously reported predictions for first-order $\Sigma\Delta$ modulators [Ref. 1].
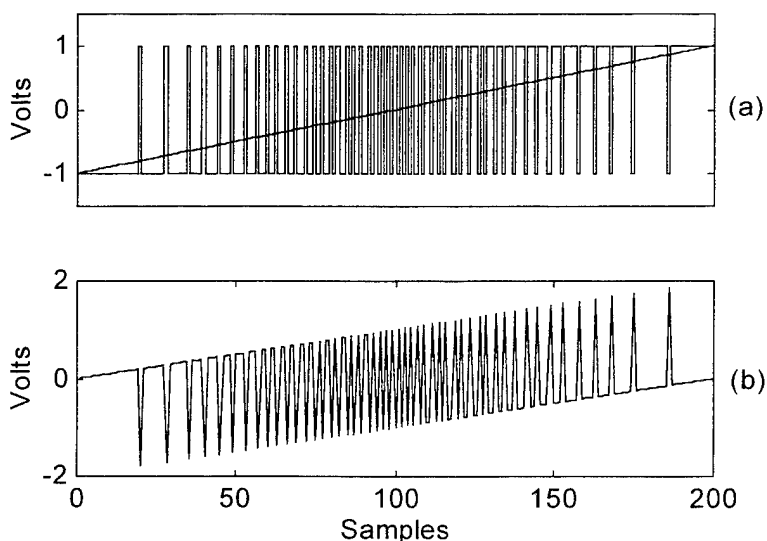
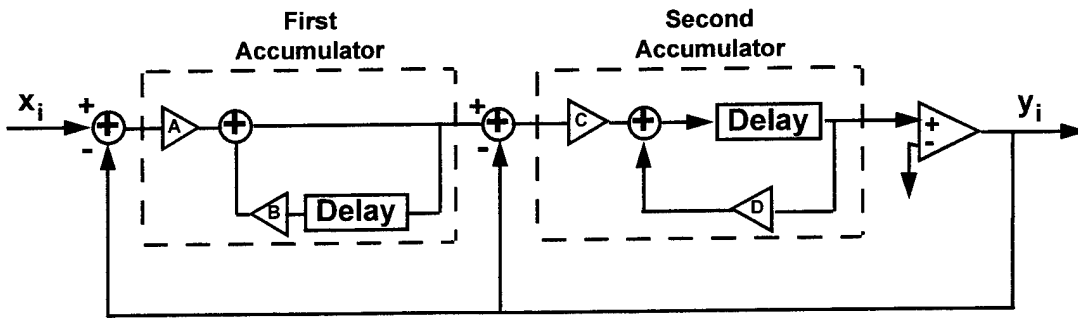**Figure 2.** 1st-order all-electronic $\Sigma\Delta M$.
(a) Plot of comparator output and sampled input.
(b) Plot of output of accumulator stage.

6

B. SECOND-ORDER ΣΔM

Although the first-order model is the simplest, the quantization noise is highly correlated to the input, resulting in excessive limit cycles. Extending the architecture to a second-order modulator eliminates a number of instabilities and increases the reliability of the circuit. However, higher-order designs (greater than 2) suffer from instability due to the undesirable limit cycles (bounded oscillations) which result in the accumulation of large signals in the integrators [Ref. 4].

A sampled-data equivalent circuit diagram of a second-order, electronic ΣΔM is shown in Figure 3.

Figure 3. Block diagram of a 2nd-order all-electronic ΣΔM.

The first accumulator, which embeds the delay in the feed-backward path, has a transfer function given by

$$H_1(z) = \frac{A}{1 - Bz^{-1}},$$ (1)

where the coefficients A and B are the gains of the system. The second accumulator stage embeds the delay in the feed-forward path. Its transfer function is given by

$$H_2(z) = \frac{Cz^{-1}}{1 - Dz^{-1}},\qquad(2)$$

where coefficients C and D are the loop system gains. For this example all coefficient values are ideally set at unity. As in the 1st-order $\Sigma\Delta$M, the comparator output voltage is ±1 volt with the threshold voltage set at zero volts.

The response of the second-order $\Sigma\Delta$M is illustrated in Figure 4. The input used for simulation consists of 200 data samples ramped from -1 volt to +1 volt in increments of 0.01 volts. The duty cycles of the quantizer output are weighted toward the average value of the input. That is, at the start of the ramped input, the duty cycles are weighted toward the bottom-level quantization (Figure 4a). Towards the center of the input, the duty cycles are at about 50%. At the high end of the ramp, they are weighted toward the top-level quantization. Figure 4b shows the signal value at the output of the accumulator stages. From the output of accumulator #1, it can be easily seen that the output is oscillating about the ramped input range of −1 to +1 volt. Results of the second-order modulator illustrate how a second feedback loop attenuates the excessive limit cycles (due to high correlation of the quantization noise) found in the first-order modulator [Ref 1].

Although not part of the current modulator investigation, a low-pass filter can then be used to resample the quantized signal at the Nyquist rate. This serves to eliminate any out-of-band quantization noise. It also determines the ratio of the sampled, quantized outputs over the Nyquist interval. This average value proves to be highly representative of the input value.

This chapter provided an overview of current sigma-delta architecture. The design and simulation of first- and second-order, all-electronic modulators were analyzed and discussed. These results provide a baseline for comparison in the design and simulation of an integrated optical sigma-delta modulator, which is discussed in the following chapter.
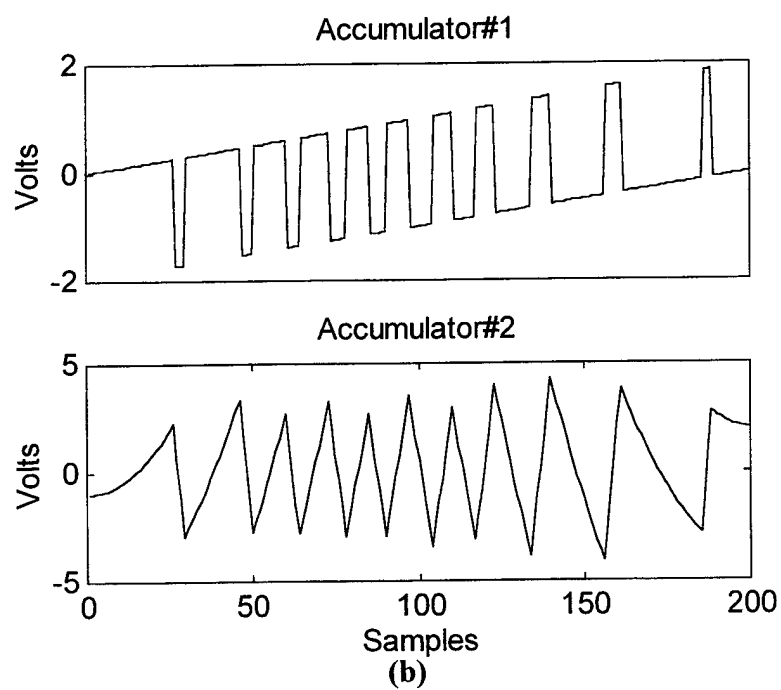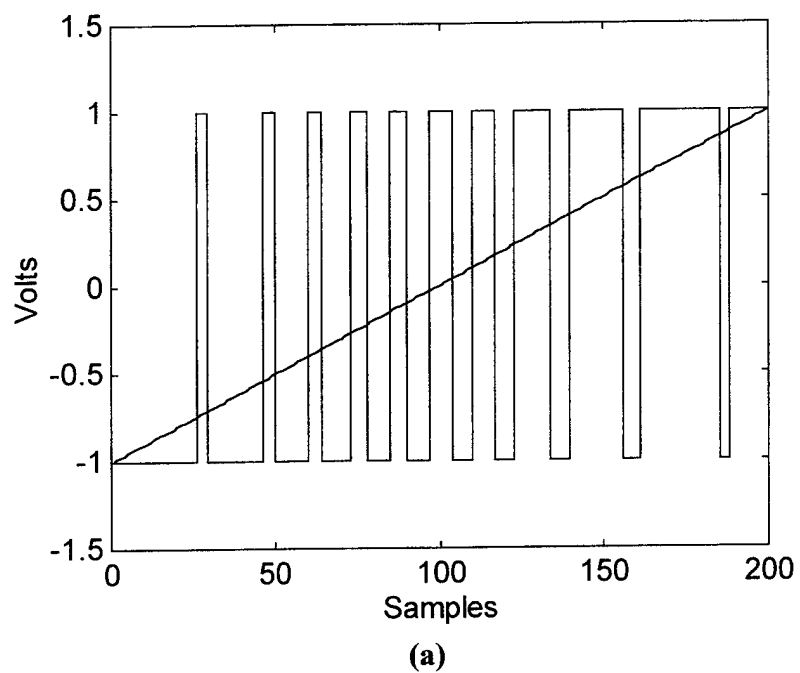
Figure 4. 2nd-order all-electronic ΣΔM.
(a) Plot of comparator output and sampled input.
(b) Plot of input at first and second accumulator stages.

III. INTEGRATED OPTICAL, SINGLE-BIT ΣΔ MODULATORS

A. FIRST-ORDER ΣΔM

A block diagram of a first-order, integrated optical ΣΔM is shown in Figure 5. In applying optical integrated components to a ΣΔ architecture, a first-order model is first simulated. In the integrated optical design, laser pulses from a mode-locked laser are used to oversample the RF signal. Mode-locked lasers are capable of providing a high pulse-repetition-frequency, narrow pulsewidths and jitter times on the order of 200 fs. In order to gain a better understanding of the model, the integrated optical components used are described in detail.

Figure 5. Block diagram of a 1st-order, integrated optical ΣΔM.

1. Mach-Zehnder Interferometer

The Mach-Zehnder interferometer (MZI) is used to efficiently couple the wideband RF signal into the optical domain. It also serves to subtract the feedback signal from the input signal. **Figure 6** shows a schematic diagram of a MZI.
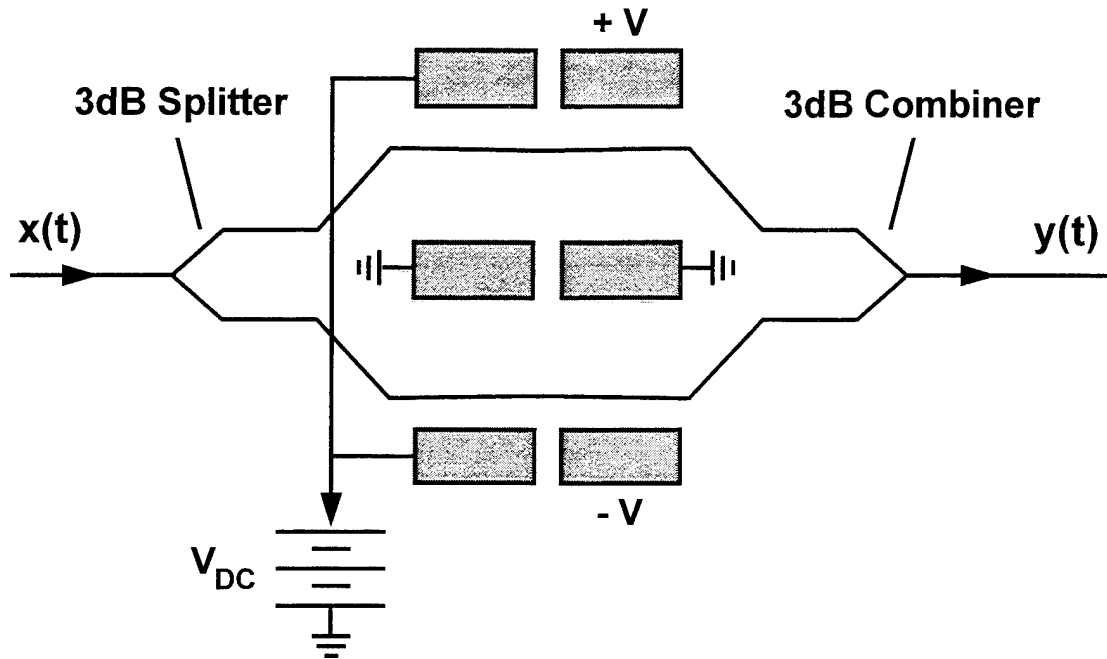
Figure 6. Schematic diagram of a Mach-Zehnder interferometer in a push-pull configuration.

The input pulse is split into equal components, each of which propagates over one arm of the interferometer. The optical paths of the two arms are equal. If no phase shift is introduced between the interferometer arms, the two components combine in phase at the output and continue to propagate undiminished. For the current design, a three-electrode configuration is used to achieve a push-pull phase change [Ref. 5]. The push-pull effect increases the phase-change efficiency of the device. This configuration is

utilized here to also subtract the feedback signal from the next input value. In order to take advantage of this push-pull configuration, the feedback voltage polarity from the comparator must be reversed. The transfer function of the MZI [Ref. 6] can be expressed as

$$I_{out} = I_{in} \left[\frac{1}{2} + \frac{1}{2} \cos(\Delta\phi(V) + \theta) \right]$$ (3)

where

$$\Delta\phi(V) = \frac{2\pi n_e^3 r \Gamma L_i V}{G\lambda}$$ (4)

is the voltage-dependent phase shift and is a function of the effective index of the optical guide n_e, the pertinent electro-optic coefficient r, the interelectrode gap G, the electrical-optical overlap parameter Γ, the DC bias θ, and the free-space optical wavelength λ. The modulation voltage, $V = V_{RF} - V_{FB}$, serves to subtract the feedback signal from the next input value. V_{RF} is the next sampled input voltage and V_{FB} is the quantized feedback voltage.

The method of accumulation involves the *magnitude* of the signal to be accumulated and the *direction* of accumulation. In the case of the first-order $\Sigma\Delta M$, two interferometers are used for the accumulator stage. One interferometer provides the *magnitude* for the accumulator. The other interferometer is used to determine the *direction* of accumulation. Figure 7 plots the transfer functions for both interferometers. Both MZIs map the input voltage to a normalized output intensity between zero and one (light intensity can not be negative). The transfer functions are the same except for the DC bias θ, which is added to the phase shift. For the MZI controlling the magnitude of the signal, $\theta = \pi$. The MZI controlling the direction of accumulation has $\theta = -\pi/2$.

As can be seen from the transfer functions, the output values for magnitude range from 0 to 0.5 and are symmetric about the input value of zero. The output values for the

13

direction range from 0 to 1. The accumulator comparator threshold voltage is normalized at 0.5 volts. The detected *direction* intensity from the MZI is compared to the normalized threshold to determine whether the intensity from the *magnitude* MZI accumulates upward or downward. The recirculating fiber lattice structure accumulates downward if the output of the interferometer is less than 0.5 and upward for values greater than 0.5. Thus the detector, comparator and optical recirculator serve to function as an accumulator.
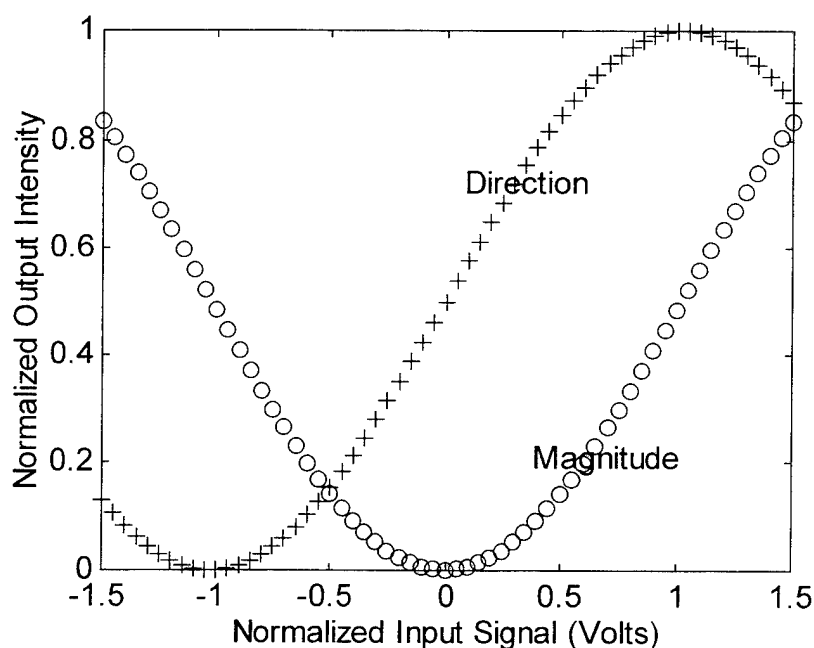

Figure 7. Transfer characteristic of the Mach-Zehnder interferometer.

2. Fiber Lattice Structures

Fiber-optic lattice structures incorporating single-mode fibers and directional couplers are used to instrument the accumulators. These fiber structures can be used to

14

perform various frequency-domain functions such as matrix operations and frequency filtering [Ref. 7]. Two structures basic to fiber signal processing include the two-coupler *nonrecirculating* and the two-coupler *recirculating* delay line. For design of the optical ΣΔ modulator, a recirculating feed-backward fiber lattice structure is utilized for the accumulator. The generalized form of a two-coupler, 4-port recirculating fiber delay line is shown in Figure 8. Moslehi *et al.* described the z-transform transfer matrix of this

Adjustable Directional Coupler
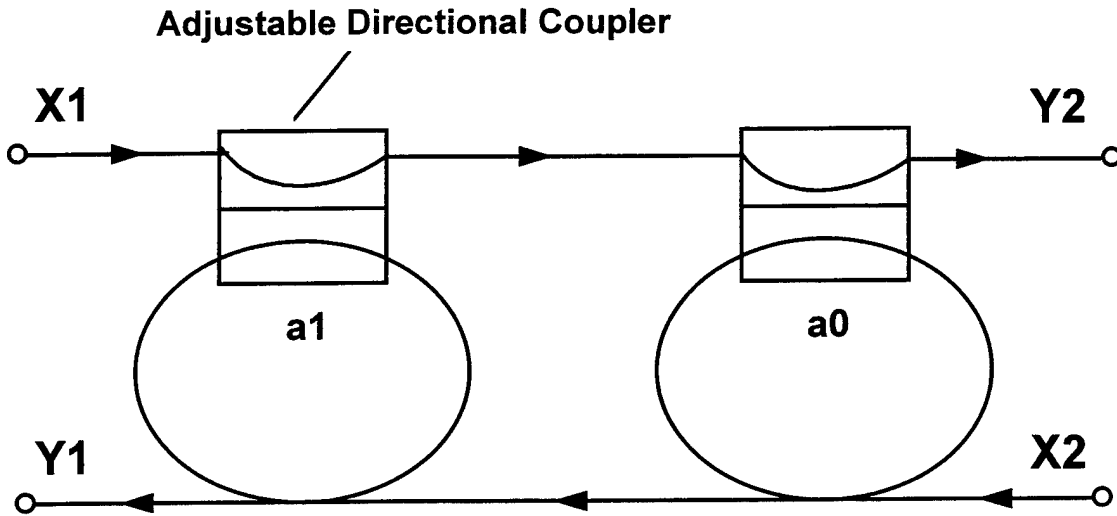
Figure 8. Block diagram of a recirculating fiber optic lattice structure.

recursive structure [Ref. 7]. The inputs and outputs are related to each other by

$$\begin{pmatrix} Y_1(z) \\ Y_2(z) \end{pmatrix} = \begin{pmatrix} H_{11}(z) & H_{12}(z) \\ H_{21}(z) & H_{22}(z) \end{pmatrix} \begin{pmatrix} X_1(z) \\ X_2(z) \end{pmatrix}. \tag{5}$$

The transfer functions within the transfer matrix are

$$H_{11}(z) = \frac{a_1 - (1 - 2a_1)a_0 L_1 z^{-1}}{1 - a_1 a_0 L_1 z^{-1}} \tag{6}$$

$$H_{21}(z) = \frac{1}{1 - a_0 a_1 L_1 z^{-1}} \tag{7}$$

$$H_{12}(z) = \frac{(1 - 2a_0 - 2a_1 + 4a_0 a_1 + a_0^2 a_1^2 + a_0^2 - 2a_0^2 a_1 + a_1^2 - 2a_1^2 a_0)L_1 z^{-1}}{1 - a_0 a_1 L_1 z^{-1}} \tag{8}$$

$$H_{22}(z) = \frac{-a_0 - a_1(1 - 2a_0)L_1 z^{-1}}{1 - a_1 a_0 L_1 z^{-1}} \tag{9}$$

and describe the use of the general structure where $H_{mn}(z)$ is the transfer function from input X_n to output Y_m. Thus $H_{21}(z)$ relates the X_1 input and Y_2 output and $H_{12}(z)$ relates the X_2 input and Y_1 output. The parameters a_0 and a_1 are the intensity coupling coefficients of the directional couplers and L_1 is the loop intensity transmittance of the system. For convenience L_1 is assumed to be one (no losses in the system). The accumulator comparator voltage is then used to bias the directional coupler (a_1) in order to create a phase change between the two pulses in order to perform the accumulation.

The accumulator stage in the first-order model has a transfer function given by Equation 2. From the transfer matrix of the recirculating fiber lattice structure, $H_{12}(z)$ matches this form where

$$C = 1 - 2a_0 - 2a_1 + 4a_0 a_1 + a_0^2 a_1^2 + a_0^2 - 2a_0^2 a_1 + a_1^2 - 2a_1^2 a_0 \tag{10}$$

and

$$D = a_0 a_1 \tag{11}$$

are the corresponding gain values. The specific lattice configuration is shown in Figure 9. The coupling coefficients a_0 and a_1 represent the percentage of light intensity coupled
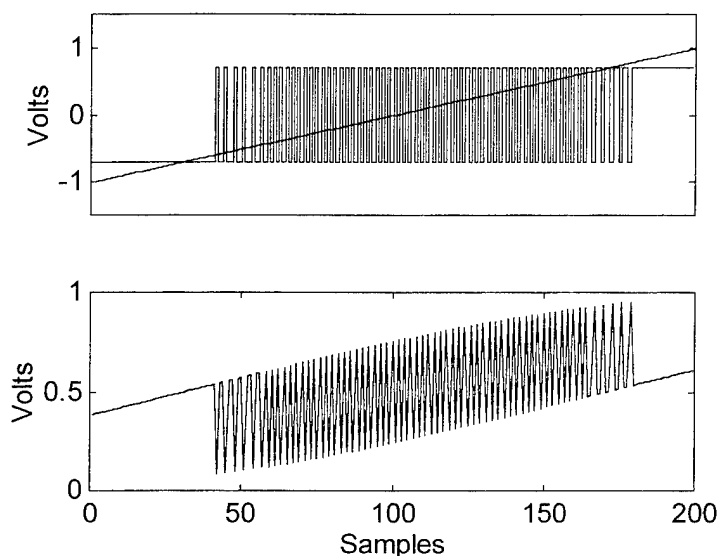
Adjustable Directional Coupler
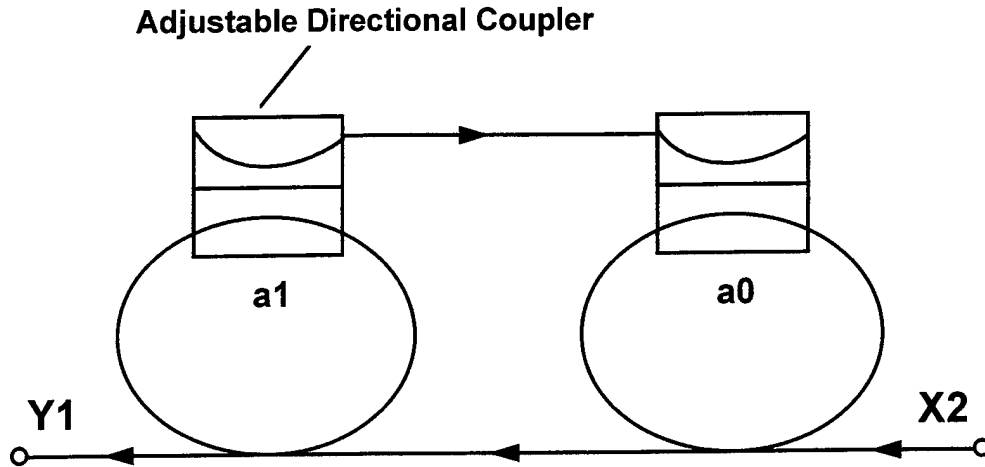
Figure 9. Block diagram of specific fiber lattice configuration used for accumulator stage with transfer function $H_{12}(z)$.

and therefore is bounded between 0 and 1. The desired values for C and D would be unity. However, the two equations work against each other simultaneously as shown in Figure 10. Here $a_0 = 0.3$ and a_1 varies from 0 to 1. Values near the intersection of C and
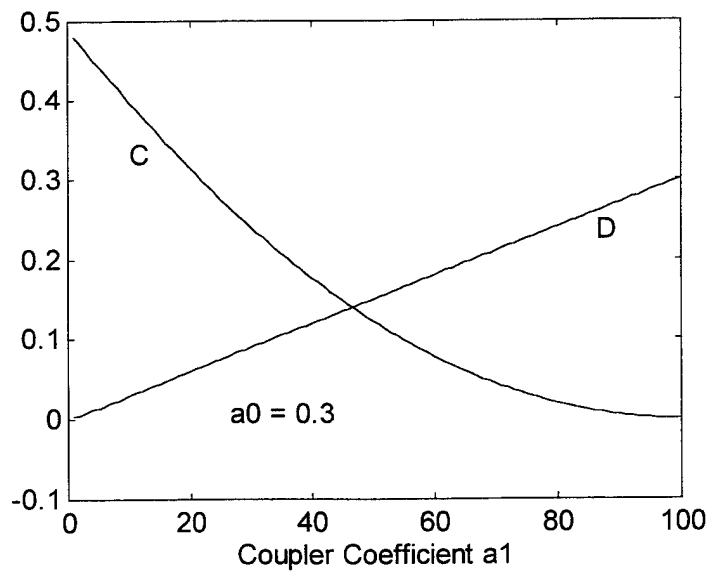
**Figure 10.** Plot of accumulator gains C and D as functions of a_0 and a_1.

D provide the best results ($a_l = 0.5$, $C = 0.122$, $D = 0.15$). In order to compensate for the small value of C, an optical amplifier with a gain of 100 is placed just prior to the fiber lattice structure in the accumulator stage (see Figure 5). Figure 11 plots the transfer characteristic of the first-order, integrated optical $\Sigma\Delta M$. It is apparent that the first-order system is not stable enough for accurate conversion of the signal due to excessive limit cycles.

Figure 11.   Transfer characteristic of 1st-order electro-optic $\Sigma\Delta M$.

B.   SECOND-ORDER ΣΔM

The block diagram for a second-order, integrated optical ΣΔM is shown in Figure 12.
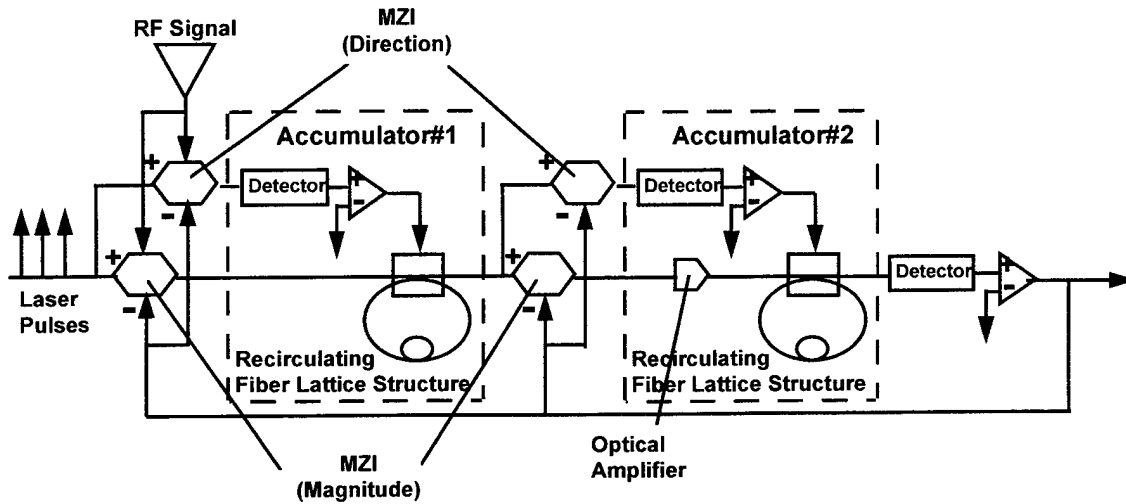
Figure 12. Block diagram of a 2nd-order electro-optic ΣΔM.

The first stage (Accumulator#1) has the transfer function described by Equation 1 and uses $H_{21}(z)$ given by Equation 7. The specific fiber lattice structure configuration used for the first accumulator stage is shown in Figure 13.

Adjustable Directional Coupler
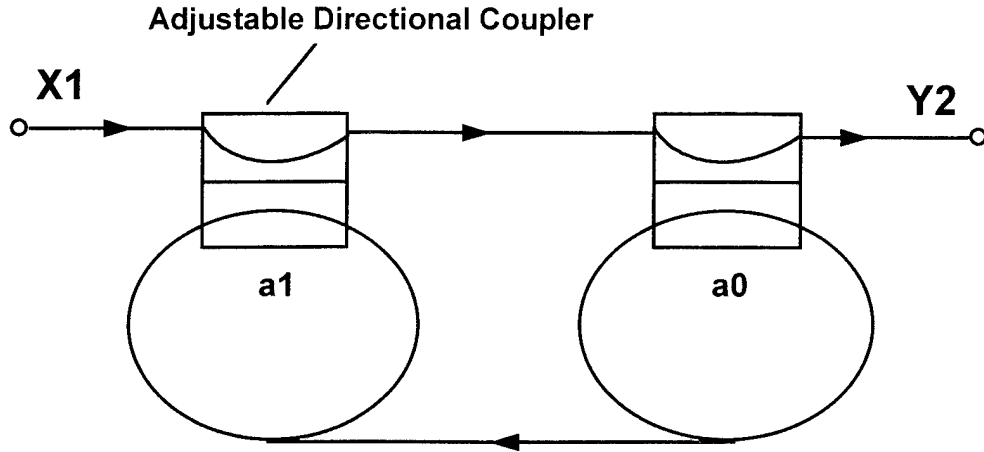
Figure 13. Block diagram of specific fiber lattice configuration used for accumulator stage with transfer function $H_{21}(z)$.

The coupler coefficients are set ideally at unity, thus the gains A and B are also set at unity. The second stage (Accumulator#2) is identical to the accumulator stage in the first-order $\Sigma\Delta M$ (see Figure 9). The coupler coefficients are again $a_0 = 0.3$ and $a_1 = 0.5$; however, the gain of the optical amplifier is now 15. The values for a_0 and a_1 were found to best optimize the accumulator gains C and D. (Appendix A provides simulation results for several other values for a_0 and a_1.)

Simulation results for the second-order, integrated optical $\Sigma\Delta M$ are plotted in Figure 14. The average value of the quantizer output can be seen to track the average value of the ramped input as shown in Figure 14a. The output of the interferometer can be seen to oscillate about the ramped input. Figure 14b plots the intermediate signal values at the input of the MZIs in the accumulator stages.

This chapter detailed the design and simulation for an integrated optical $\Sigma\Delta M$. Results for both first- and second-order modulators were analyzed. These results compared favorably to those of the all-electronic design and demonstrated the feasibility of the integrated optical approach. The next chapter discusses the effects of signal-to-noise ratio and oversampling ratio of on the bit resolution of $\Sigma\Delta M$s.
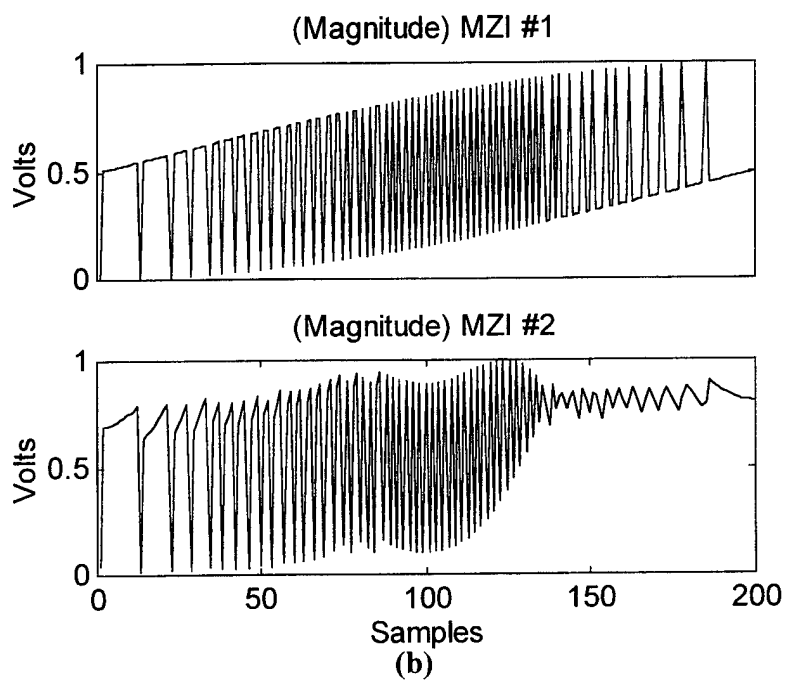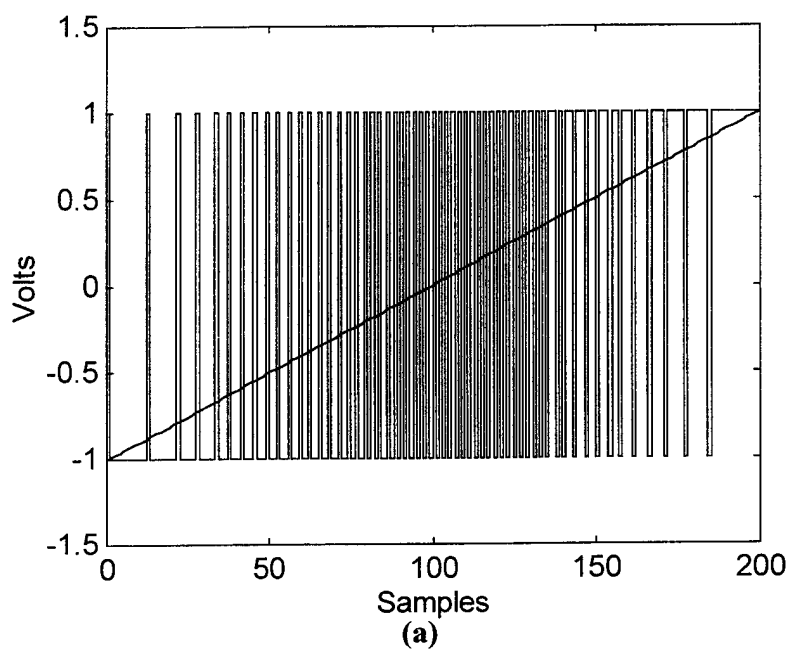
Figure 14. 2nd-order electro-optic ΣΔM.
(a) Plot of comparator output and sampled input.
(b) Plot of input at first and second accumulator stages.

IV. OVERSAMPLING RATIO AND RESOLUTION

The quantization utilized in $\Sigma\Delta M$ introduces noise in the modulator. The quantization error e is treated as white noise having probability of lying anywhere in the range $\pm\Delta/2$, where Δ is the level spacing (normalized units) between quantized levels. Its mean square value is given by [Ref. 1]

$$e_{rms}^2 = \frac{1}{\Delta}\int_{-\Delta/2}^{+\Delta/2} e^2 de = \frac{\Delta^2}{12}. \tag{12}$$

The oversampling ratio (OSR), defined as the ratio of the sampling frequency f_s to the Nyquist rate $2f_0$, is given by the integer

$$OSR = \frac{f_s}{2f_0} = \frac{1}{2f_0\tau}. \tag{13}$$

The noise power in the signal band can be shown to be [Ref. 1]

$$n_0^2 = \int_0^{f_0} e^2(f)df = e_{rms}^2(2f_0\tau) = \frac{e_{rms}^2}{OSR}. \tag{14}$$

It is evident that oversampling reduces the in-band rms quantization noise n_0 by the square root of the OSR.

The feedback loops in the $\Sigma\Delta M$ help shape the spectrum of the modulation noise by moving most of the noise outside the signal band. The filters used in the loops reduce the net noise in the signal band. The $\Sigma\Delta M$ subtracts the previous value of the quantization error from the present error. In the case of two feedback loops, the

modulation noise becomes the second difference of the quantization error. The signal-to-noise ratio for a second-order $\Sigma\Delta M$ can be predicted from [Ref. 1]

$$\frac{n_0}{\Delta} = \frac{\pi^2}{\sqrt{60}}(OSR)^{-\frac{5}{2}}.$$

(15)

For a second-order $\Sigma\Delta M$, the signal-to-noise ratio (SNR) increases at 15 dB/octave and 6 dB/bit. Thus for OSR = 128 and $\Delta = 2$, $n_0 = -97$ dB. For a signal strength of one (i.e., 0 dB), SNR $= -n_0 = 97$ dB. At 6 dB/bit, this translates to 16 bits of resolution.

For example, the resolution of the second-order, integrated optical $\Sigma\Delta M$ can be determined using the above method. Assuming the 200 input data points are sampled over one second ($f_0 = 1$ Hz), the oversampling ratio then becomes

$$OSR = \frac{f_s}{2f_0} = \frac{200}{2(1\text{Hz})} = 100.$$

(16)

Normalizing to a signal strength of one, SNR $= -n_0 = 91$ dB, which translates to 15 bits of resolution.

When discussing ADC architectures, it is important to analyze how bit resolution is determined. This chapter discussed in detail how bit resolution of $\Sigma\Delta Ms$ is affected by the SNR and oversampling ratio. Bit resolution is proven to be a function the oversampling ratio. The following chapter describes the computer software utilized to simulate modulator designs.

V. SIMULATION TOOLS

In simulating the $\Sigma\Delta$ modulators, MATLAB's SIMULINK toolbox was used. SIMULINK is a program for simulating dynamic systems. It is an extension of MATLAB and uses block diagrams to represent dynamic systems. The purpose of this chapter is to familiarize the reader with SIMULINK and how simulation results were obtained. Figure 15 shows the system block diagram for the first-order, all-electronic $\Sigma\Delta M$. The simulation variables *input*, *sum1*, *ac1* and *output* are are used for plotting simulation results. Appendix B lists the MATLAB functions and variables used in SIMULINK.
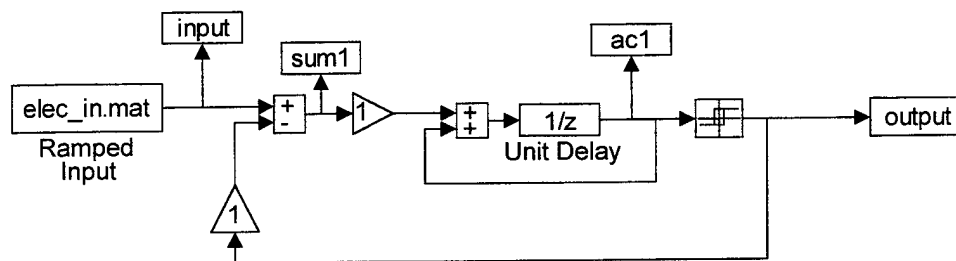
Figure 15. SIMULINK diagram of 1st-order, all-electronic $\Sigma\Delta M$ (filename el1.m).

The ramped input is a MATLAB vector (elec_in.mat) of 200 data values from -1 to $+1$ incremented at 0.01. This input is used for all simulations. The unit delay is described by the z-domain transfer function $1/z$ and is embedded in a feedback loop. The relay block is a binary switch that outputs a $+1$ if the input is above zero and -1 if the input is below zero.

The second-order, all-electronic $\Sigma\Delta M$ is modeled in much the same fashion, except that a second feedback loop is added (see Figure 16). The system gains are set at unity for simulation purposes.
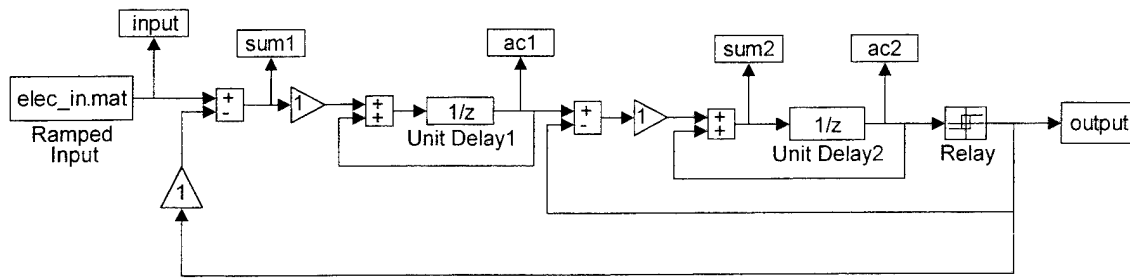
Figure 16. SIMULINK diagram of 2nd-order, all-electronic $\Sigma\Delta M$ (filename el2.m).

The SIMULINK block diagram used to model a first-order, optical integrated $\Sigma\Delta M$ is shown in Figure 17. The input vector (*optic_in.mat*) is identical to that of the all-electronic model.
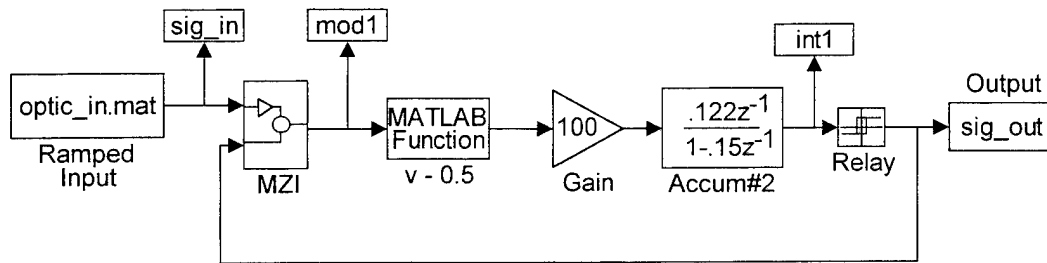
Figure 17. SIMULINK diagram of 1st-order, optical integrated $\Sigma\Delta M$ (filename op1.m).

The MZI block, unmasked in Figure 18, is used to subtract the two inputs and map the the input according to the interferometer transfer characteristic (Equation 3). The MATLAB code for the function describing the interferometer (MZI) is listed in Appendix B. After the signal is mapped to a value between zero and one, another MATLAB function (v-0.5) is used to subtract 0.5 from the input (v). The subtraction is done to normalize the signal about zero in order for the discrete integrators to function properly.
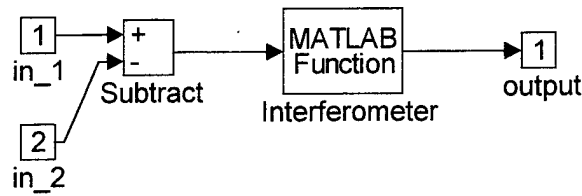
Figure 18. Unmasked MZI block from Figure 17.

The signal then passes through a gain stage of 100 before entering the integrator/accumulator. The integrator is basically a filter which can be describe by z-domain characteristics. The coefficients for this filter was described in detail in Chapter IV. Finally, the relay used is the same switch used in the all-electronic simulation model.

Figure 19 shows the SIMULINK block diagram of the second-order, optical integrated $\Sigma\Delta$M. All functional blocks are identical to the first-order model with the exception of the filters (Accum#1 and Accum#2). The coefficients for these discrete-time filters are described in Chapter IV.
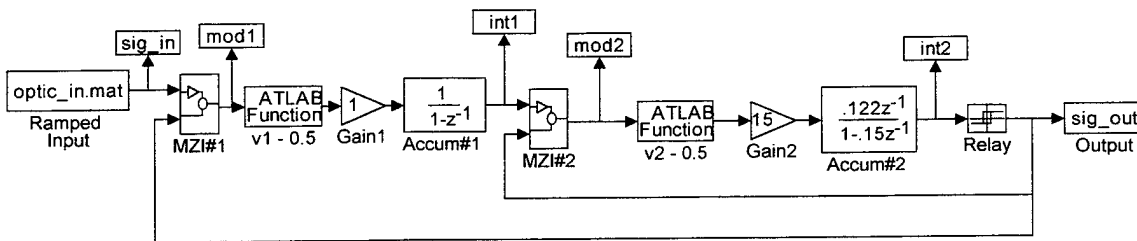
Figure 19. SIMULINK diagram of 2nd-order, optical integrated $\Sigma\Delta$M (filename op2.m).

This chapter described the use of computer simulation software (MATLAB and SIMULINK) used to design and simulate all $\Sigma\Delta$ modulators in the thesis. The figures provide system block diagrams and filenames used in obtaining simulation results. The final chapter discusses the current design and suggest recommendations for future efforts.

27

VI. CONCLUSIONS

The $\Sigma\Delta$ oversampling A/D modulator architecture uses limit cycles in quantized feedback loops to provide an accurate digital representation of the input signal. The second-order $\Sigma\Delta M$ provides a stable and robust design that is highly tolerant of circuit imperfections and component mismatch. The major limitations of this method are fast cycle times and bandwidth. The use of fiber optic technology has the potential of eliminating these limitations. An integrated optical second-order $\Sigma\Delta$ architecture allows the processing of wideband RF signals. The integrated optical $\Sigma\Delta M$ design presented in this paper is a fairly straight-forward extension of the electronic design using standard integrated optical devices. Current simulation results confirm design feasibility.

Future efforts include further optimization of the current integrated optical design. Modifications may include the possibility of optimizing the magnitude and direction of each accumulation stage using only one interferometer. The accumulation stages of the integrated optical $\Sigma\Delta M$ are modeled by fiber lattice structures with similar system transfer functions. More rigorous modeling of these delay line structures and analysis of the optical amplifiers are needed for future hardware implementation. Since the output of the modulator represents the input signal together with modulation noise, there is still a need to decimate the modulated signal. A multi-stage decimation is needed to lower the word rate and remove high-frequency modulation noise before the signal is resampled at the Nyquist rate. Design issues to be studied include nonlinearities associated with interferometers, stability of the accumulator stages, effects of net gains in the feedback loops, and the effects of modulation noise and oversampling frequency (OSR) on bit resolution.

REFERENCES

[1] J.C. Candy and G.C. Temes, "Oversampling methods for A/D and D/A conversion," J.C. Candy and G.C. Temes, editors, *Oversampling Delta-Sigma Data Converters*, IEEE Press, pp. 1-29, 1992.

[2] J.C. Candy, "A use of limit cycle oscillations to obtain robust analog-to-digital converters," *IEEE Trans.Commun.*, vol. COM-22, pp. 298-305, Mar. 1974.

[3] C.C. Cutler, "Transmission systems employing quantization," 1960 U.S. Patent No. 2,927,962 (filed 1954).

[4] B.E. Boser and B.A. Wooley, "The design of sigma-delta modulation analog-to-digital converters," *IEEE J. Solid-State Circuits*, vol. 23, no. 6, pp. 1298-1308, Dec. 1988.

[5] R. C. Alferness, "Waveguide electrooptic modulators," *IEEE Trans. Microwave Theory Tech.*, vol. MTT-30, no. 8, pp. 1121-1137, Aug. 1982.

[6] P.E. Pace, S.J. Ying, J.P. Powers and R.J. Pieper, "Optical SD analog-to-digital converters for high-resolution digitization of antenna signals," *Proc. PSAA-V Fifth Annual ARPA Symposium on Photonic Systems For Antenna Applications*, pp. 412-416, Jan. 1995.

[7] B. Moslehi, J.W. Goodman, M. Tur and H.J. Shaw, "Fiber-optic lattice signal processing," *Proc. IEEE*, vol. 72, no. 7, pp. 909-930, Jul. 1984.

APPENDIX A: SIMULATION RESULTS

The following figures provide further simulation results for the second-order, optical integrated ΣΔM using several other values for the directional coupler coefficients (a_0 and a_1). These results are provided to illustrate the sensitivity of the system to the coefficient settings.
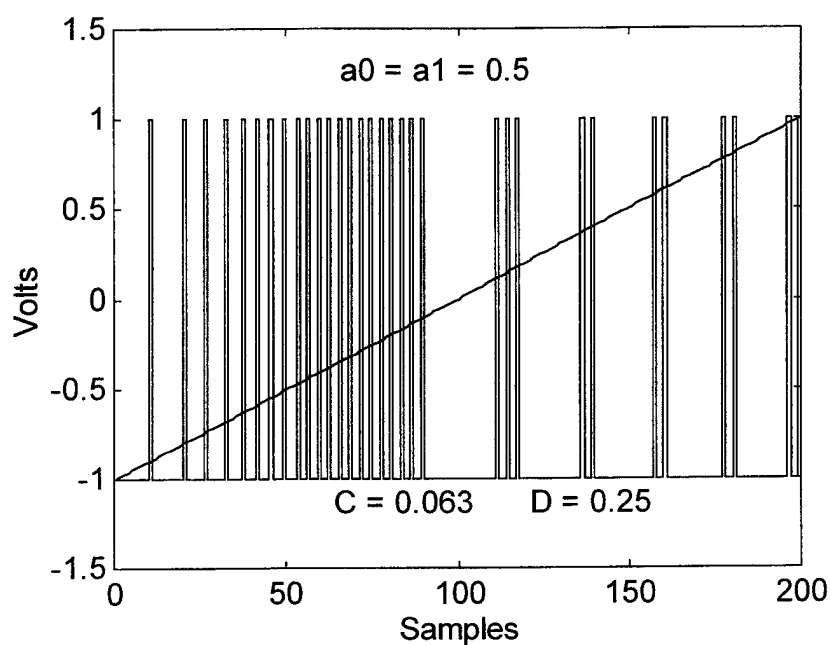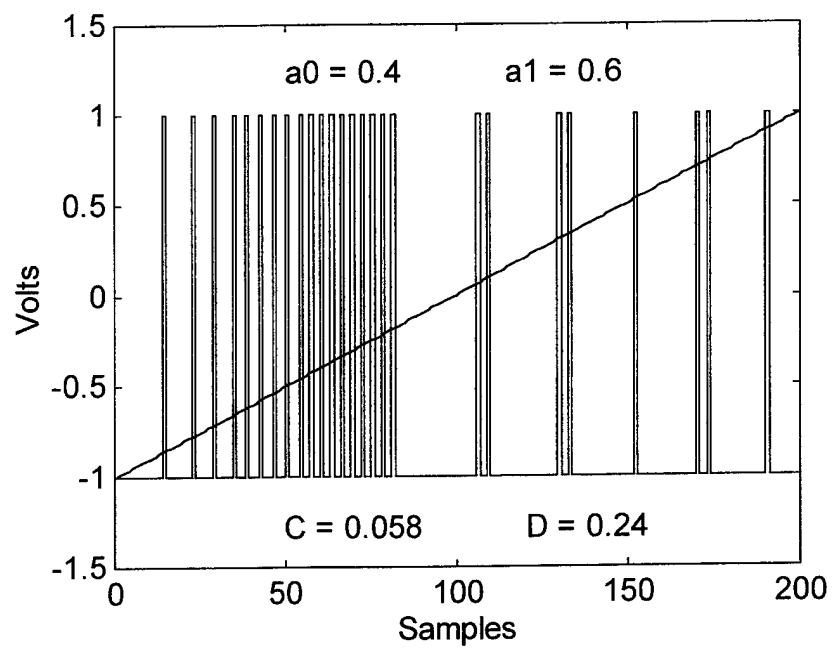

Figure 20. Plot of output and input with gains $C = 0.063$ and $D = 0.25$.
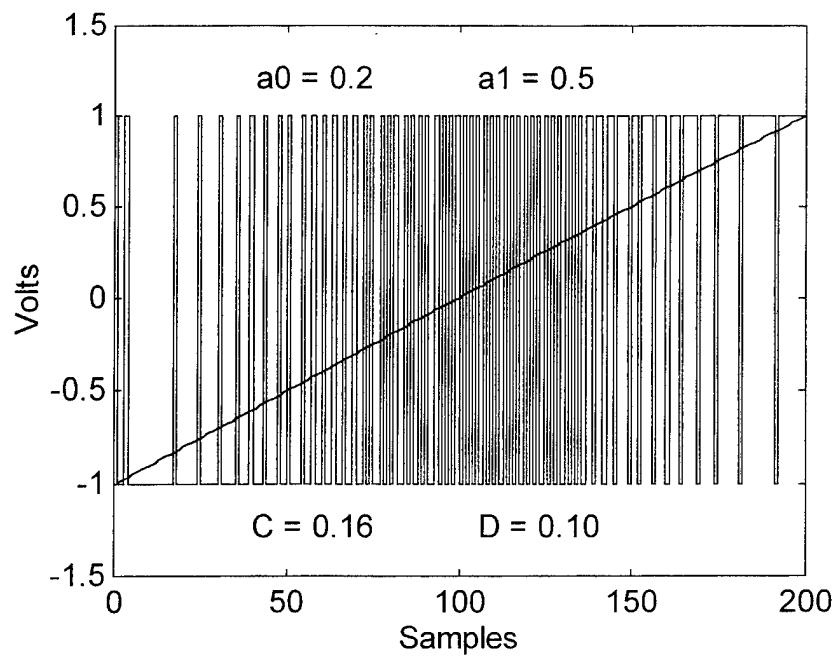
Figure 21. Plot of output and input with gains $C = 0.16$ and $D = 0.10$.
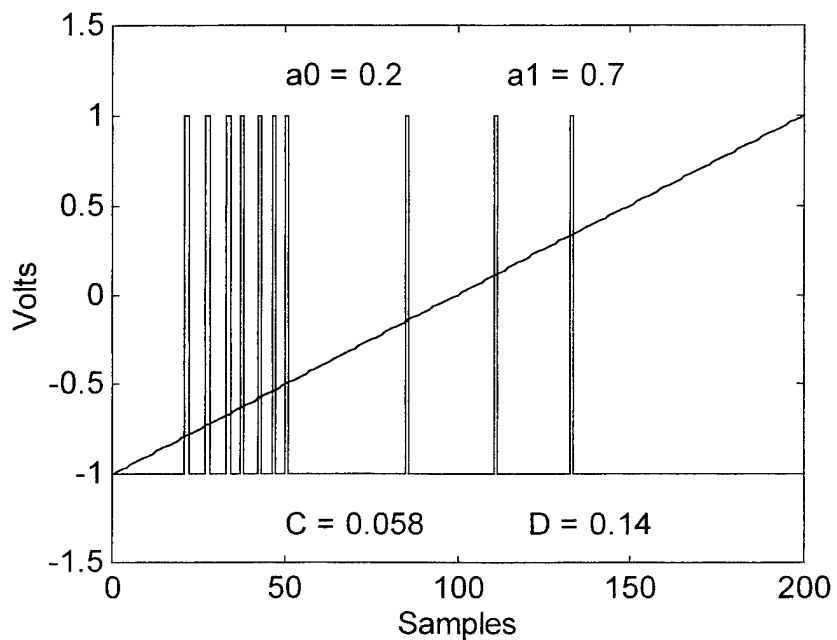
Figure 22. Plot of output and input with gains $C = 0.058$ and $D = 0.14$.

Figure 23. Plot of output and input with gains $C = 0.058$ and $D = 0.24$.

APPENDIX B: MATLAB CODE USED IN SIMULINK

FILENAME interfer.m
```
% INTERFEROMETER TRANSFER FUNCTION  (Equation 3)
function I_out=interfer(v)

G=3.0e-6;          % Gap (m)
wl=0.9e-6;         % wavelength (m)
n=2.205;           % index
r=30.8e-12;        % electro-optic coefficient (v/m)
GAMMA=0.5;          % overlap integral
L=0.0020;          % length (m)
V_rf=0;
Vs=0;
phase=-pi/2;
K=(2*pi*n^3*r*GAMMA*L)/(G*wl);
I_out=(.5 + .5*cos(K*v + phase));
```

FILENAME el_ramp.m
```
% Input ramp vector for both electronic and optical models

limit=1;
V_rf=[-limit:.01:limit];
t=[0:limit*200];
V_in=[t;V_rf];
input=V_in;
save elec_in input
```

FILENAME el1_plot.m
```
% Plots el1.m output (First-Order, All-Electronic Model)

save el1_out sum1 input output   % Saves simulation variables for plot

clear
limit=1;
```

```
figure(1)  % First figure plots input and output
clg
load el1_out
subplot(2,1,1),plot(input,'c'),hold,stairs(output)
set(get(gca,'Chil'),'color','red')
ylabel('Volts')
axis([0 limit*200 -1.5 1.5])
set(gca,'xtick',[]);
subplot(2,1,2),plot(sum1,'c')
axis([0 limit*200 -limit-1 (limit+1)])
ylabel('Volts'),xlabel('Samples')
```

FILENAME el2_plot.m
```
%  Plots el2.m outputs (Second-Order, All-Electronic Model)

save el2_out sum1 ac1 sum2 ac2 input output  % Saves simulation variables for plot

clear
limit=1;

figure(1)      % First figure plots input and output
clg
load el2_out
plot(input,'c'),hold,stairs(output)
set(get(gca,'Chil'),'color','red')
ylabel('Volts'),xlabel('Samples')
axis([0 limit*200 -1.5 1.5])

figure(2)      % Second figure plots intermediate stages
subplot(2,1,1),plot(sum1,'r'),title('Accumulator#1')
ylabel('Volts')
set(gca,'xtick',[]);
subplot(2,1,2),plot(sum2,'r'),title('Accumulator#2')
ylabel('Volts')
xlabel('Samples')
```

FILENAME op1_plot.m
% Plots op1.m outputs (First-Order, Optical Integrated Model)

% Save simulation variables for plot
save op1_out mod1 int1 sig_in sig_out

```
clear
limit=1;
figure(1)
clg
load op1_out
subplot(2,1,1),plot(sig_in,'c'),hold,stairs(sig_out)
ylabel('Volts')
set(get(gca,'Chil'),'color','r')
set(gca,'xtick',[]);
axis([0 limit*200 -limit-.5 limit+.5])
subplot(2,1,2),plot(mod1,'c')
ylabel('Volts'),xlabel('Samples')
```

FILENAME op2_plot.m
% Plots op2.m outputs (Second-Order, Optical Integrated Model)

```
save op2_out mod1 int1 mod2 int2 sig_in sig_out
clear
limit=1;
figure(1)
clg
load op2_out
plot(sig_in,'c'),hold,stairs(sig_out)
set(get(gca,'Chil'),'color','red')
ylabel('Volts'),xlabel('Samples')
axis([0 limit*200 -limit-.5 limit+.5])
figure(2)
subplot(2,1,1),plot(mod1,'r'),title('(Magnitude) MZI #1')
ylabel('Volts')
set(gca,'xtick',[]);
subplot(2,1,2),plot(mod2,'r'),title('(Magnitude) MZI #2')
ylabel('Volts')
xlabel('Samples')
```

FILENAME mzi.m
```
%  Plots MZI transfer characteristics
clear

G=3.0e-6;          % Gap (meter)
wl=0.9e-6;         % wavelength (meter)
n=2.205;           % index
r=30.8e-12;        % electro-optic coefficient (v/m)
GAMMA=0.5;           % overlap integral
L=0.0040;          % length (m)


V_rf=0;
Vs=0;
sign=-pi/2;
mag=pi;


vpi=G*wl/(2*L*n^3*r*GAMMA)


v=[-1.5:.05:1.5];


K=(2*pi*n^3*r*GAMMA*L)/(G*wl);


for i=1:61
  I_sign(i)=(.5 + .5*cos(K.*v(i) + sign));
end


for j=1:61
  I_mag(j)=(.5 + .5*cos(K.*v(j) + mag));
end


clg
plot(v,I_sign,'r+'),hold,plot(v,I_mag,'co')
xlabel('Normalized Input Signal (Volts)')
ylabel('Normalized Output Intensity')
```

FILENAME lattice.m (Equations 10 and 11)
% Plots coefficients for Lattice transfer function

```
clear
inc = 0.01;
C = zeros(1,inc*10000);
D = zeros(1,inc*10000);

a0 = .3;
L1 = 1;

for a1 = .01:inc:1.00
    C(a1*100) = (1-2*a0-2*a1+4*a1*a0+a1^2*a0^2+a0^2-2*a0^2*a1...
+a1^2-2*a1^2*a0)*L1;   % These two lines constitute one equation

    D(a1*100) = a0*a1*L1;
end

clg
plot(C,'c-'),hold,plot(D,'r-')
xlabel('Coupler Coefficient a1')
```

INITIAL DISTRIBUTION LIST

1. Defense Technical Information Center   2
    Cameron Station
    Alexandria, VA 22304-6145

2. Dudley Knox Library, Code 013   2
    Naval Postgraduate School
    Monterey, CA 93943-5101

3. Chairman, Code EC   1
    Department of Electrical and Computer Engineering
    Naval Postgraduate School
    Monterey, CA 93943-5121

4. Prof. P.E. Pace, Code EC/Pc   2
    Department of Electrical and Computer Engineering
    Naval Postgraduate School
    Monterey, CA 93943-5121

5. Prof. J.P. Powers, Code EC/Po   1
    Department of Electrical and Computer Engineering
    Naval Postgraduate School
    Monterey, CA 93943-5121

6. Prof. R.J. Pieper, Code EC/Pr   1
    Department of Electrical and Computer Engineering
    Naval Postgraduate School
    Monterey, CA 93943-5121

7. LT Stephen J Ying   2
    6677 Renwood Rd
    Independence, OH 44131

8. Richard Becker   1
    Integrated Optical Circuit Cons.
    10482 Chisholm Ave.
    Cupertino, CA 95014

9.   Gary Betts   1
        MIT Lincoln Lab
        PO Box 73, MS: C-225
        Lexington, MA 02173-9108

10.   Catherine Bulmer   1
        Naval Research Lab
        455 Overlook Ave., S.W.
        Code 6571
        Washington, DC 20375-5320

11.   William Burns   1
        Naval Research Lab
        455 Overlook Ave., S.W.
        Code 6571
        Washington, DC 20375-5320

12.   Donald LaFaw   1
        Laboratory for Physical Sciences
        8050 Greenmead Dr.
        College Park, MD 20740

13.   Michael VanBlaricum   1
        Toyon Research Corporation
        75 Aero Camino, Suite A
        Goleta, CA 93117-3139